Parallel finite volume simulation of the spherical shell dynamo with pseudo-vacuum magnetic boundary conditions

Liang Yin[a,b], Chao Yang[c,*], Shi-Zhuang Ma[b], Ying Cai[d], Keke Zhang[a]

[a]*State Key Laboratory of Lunar and Planetary Sciences, Macau University of Science and Technology, Macau, China*
[b]*School of Engineering Science, University of Chinese Academy of Sciences, Beijing 100049, China*
[c]*School of Mathematical Sciences, Peking University, Beijing 100871, China*
[d]*Institute of Applied Physics and Computational Mathematics, Beijing 100094, China*

Abstract

In this paper, we study the parallel simulation of the magnetohydrodynamic (MHD) dynamo in a rapidly rotating spherical shell with pseudo-vacuum magnetic boundary conditions. A second-order finite volume scheme based on a collocated quasi-uniform cubed-sphere grid is applied to the spatial discretization of the MHD dynamo equations. To ensure the solenoidal condition of the magnetic field, we adopt a widely-used approach whereby a pseudo-pressure is introduced into the induction equation. The temporal integration is split by a second-order approximate factorization approach, resulting in two linear algebraic systems both solved by a preconditioned Krylov subspace iterative method. A multi-level restricted additive Schwarz preconditioner based on domain decomposition and multigrid method is then designed to improve the efficiency and scalability. Accurate numerical solutions of two benchmark cases are obtained with our code, comparable to the existing local method results. Several large-scale tests performed on the Sunway TaihuLight supercomputer show good strong and weak scalabilities and a noticeable improvement from the multi-level

[*]Corresponding author

Email addresses: `lyin@must.edu.mo` (Liang Yin), `chao_yang@pku.edu.cn` (Chao Yang), `szma@ucas.edu.cn` (Shi-Zhuang Ma), `cai_ying@iapcm.ac.cn` (Ying Cai), `K.Zhang@exeter.ac.uk` (Keke Zhang)

preconditioner with up to 10368 processor cores.

1. Introduction

The magnetic field of the Earth as well as many other planets is widely thought to be generated by the convection of the electrically conducting fluid in the outer core, which creates the so-called self-excited dynamo action (Zhang and Schubert, 2000; Christensen and Wicht, 2007; Wicht and Tilgner, 2010; Jones, 2011; Roberts and King, 2013; Moffatt and Dormy, 2019; Deguen and Lasbleis, 2020). Due to a series of reasons (Aurnou et al., 2015; Vantieghem et al., 2016), it is a challenging task to fully understand the dynamics in planetary fluid cores. Starting with the pioneering work by Glatzmaier and Roberts (1995), Kageyama and Sato (1995) and Kuang and Bloxham (1997), significant progresses have been made in understanding of the origin and evolution of the Earth's magnetic field by means of numerical dynamo simulations (Sheyko et al., 2016; Christensen, 2018; Petitdemange, 2018; Aubert, 2019). Although there has been a number of numerical codes for dynamo modelling developed independently by various groups (Matsui et al., 2016), there is still a long way from achieving dynamo simulations with physically realistic parameters, due mainly to the difficulties in extreme-scale spatial resolutions (Glatzmaier, 2002; Jones, 2011; Roberts and King, 2013; Aurnou et al., 2015). Tremendous amounts of computing resources are required for such extreme-resolution dynamo simulations, which can only be made possible with the aid of massively parallel supercomputers (Harder and Hansen, 2005; Chan et al., 2006). Innovations in the numerical algorithms and their applications on massively parallel supercomputers are likely beneficial to extend the parameter regime in dynamo simulations towards more realistic values relevant to the planetary cores (Matsui and Okuda, 2002, 2004a; Harder and Hansen, 2005; Chan et al., 2006, 2007; Matsui et al., 2016).

As reported in Matsui et al. (2016), a majority of the existing widely-used numerical dynamo models employ global-nature spectral methods, which are based on the poloidal-toroidal decomposition and spherical harmonic expansions. The solenoidal condition of the velocity and magnetic field and the insulating boundary condition for the magnetic field can be easily dealt with in such methods. However, a significant number of global communications are usually required for the computation of nonlinear terms, which could make spectral methods less suitable for large-scale parallel computations (Harder and Hansen, 2005; Chan et al., 2006, 2007; Wicht et al., 2009). Besides, spectral methods are often hard to be adapted to more complicated domains without a spherical symmetry (Iskakov et al., 2004; Vantieghem et al., 2016). In contrast, local discretization approaches, such as finite volume and finite element methods, show more potentials for parallel computations and could be more flexible to complicated domains, thus are bringing an increasing interest in dynamo simulations (e.g. Kageyama and Sato, 1995, 1997; Hejda and Reshetnyak, 2003, 2004; Kageyama and Yoshida, 2005; Harder and Hansen, 2005; Matsui and Okuda, 2002, 2004a,b, 2005; Chan et al., 2001a,b, 2006, 2007; Vantieghem et al., 2016; Yin et al., 2017, 2019). However, the applications of the local methods in dynamo simulations still face several difficulties, such as: (i) the solenoidal conditions of the velocity and magnetic field, (ii) the insulating boundary condition for the magnetic field, and (iii) parallel scalability. To cope with the solenoidal constraint, most of the dynamo simulations adopt a projection-based method introduced by Tóth (2000), in which a pseudo-pressure gradient is added into the induction equation and the pseudo-pressure is interpreted as an effecting projection of the provisional magnetic field onto the solenoidal space, just as the pressure in momentum equation. This method has been applied successfully to a large number of dynamo models (e.g. Chan et al., 2001a; Harder and Hansen, 2005; Chan et al., 2007; Vantieghem et al., 2016).

The exterior space outside the Earth's core is generally thought as an electrically insulating medium, resulting in a non-local nature of the magnetic boundary condition since the solution of a Laplace equation for the magnetic scalar

potential in the infinite exterior domain is theoretically required. This insulating boundary condition brings substantial difficulties in dynamo simulations with local methods. A straightforward approximation is to replace the infinite exterior extent with a finite domain since the magnetic scalar potential declines as $O(r^{-2})$ in the insulating exterior and can be approximated as zero at the location far enough from the fluid domain of interest. Based on this approximation, several dynamo models with local methods treat the insulating boundary condition via an extra numerical cost in a finite exterior domain. Examples include Chan et al. (2001a) and Chan et al. (2007) in which a weak conductivity approximation is introduced and Matsui and Okuda (2005) where a formulation of the magnetic vector potential is used. Another approach is to introduce a mathematically equivalent boundary integral formulation proposed by Iskakov et al. (2004), in which the 3-D Laplace equation for the magnetic potential is recast as a 2-D integral equation on the boundary surface next to the insulating medium. However, such approach usually leads to a higher computational cost due to the dense coefficient matrix and the global communication between all processors handling the boundary points. On the other hand, pseudo-vacuum boundary conditions, which prescribe the tangential component of the magnetic field on the boundary to be zero, since first adopted by Kageyama and Sato (1995) in their finite difference code, have become a popular alternative. Implementation of such conditions in local methods is straightforward and no extra numerical cost or global communication is required. Though these conditions may result in quite different numerical solutions from the insulating condition (Harder and Hansen, 2005; Jackson et al., 2014), it may be quite suitable to apply them to the benchmark studies, as was done in Jackson et al. (2014) and Vantieghem et al. (2016), thus providing a convenient way to validate dynamo codes with local methods.

The parallel scalability, which is the key limiting factor for the massive-scale simulations, is frequently investigated in dynamo simulations to different degrees (e.g. Harder and Hansen, 2005; Chan et al., 2006, 2007; Vantieghem et al., 2016). In particular, parallel performance benchmarks from 15 widely-

4

used parallel dynamo models are thoroughly reported by Matsui et al. (2016) but only two codes based on local methods are included therein. While local methods show great potentials for the massive-scale dynamo simulations, the study on improving the parallel scalability of local codes is still of critical importance. The temporal integration in the projection-based local models generally involves a fractional step algorithm consisting of a prediction procedure and a correction step. In practice, most of the computing time in the temporal integration is spent on the numerical solution of the pressure Poisson equation in the correction step (Harder and Hansen, 2005; Vantieghem et al., 2016; Yin et al., 2017). To improve the parallel performance of this type of code, the design of a scalable solver for the prediction equation and especially for the pressure Poisson equation is highly desirable.

In this work, we present a parallel finite volume solution for the convection-driven magnetohydrodynamic (MHD) dynamo in a rapidly rotating spherical shell with pseudo-vacuum magnetic boundary conditions. As a continuation to our previous work (Yin et al., 2017) on the non-magnetic convection problem, this paper inherits the approximate factorization method in temporal integration and the finite volume scheme on a collocated quasi-uniform cubed-sphere grid, and focuses on the algorithms and implementations related to the magnetic field. In addition to that, efforts have also been made on the design of a multi-level restricted additive Schwarz preconditioner based on domain decomposition and multigrid method to improve the efficiency and scalability. It is worth mentioning that the adopted cubed-sphere grid can be easily extended to ellipsoidal shell domains and, in theory, other geometries which can be expressed by a similar projection relationship.

The remainder of the paper is organized as follows. We first present the governing equations for the MHD dynamo problem and the boundary conditions in Section 2. Then in Section 3, we introduce the numerical methods including the temporal integration, spatial discretization and parallel multi-level solver. The numerical results about the validation and parallel performance are reported in Section 4. We conclude the paper in Section 5.

5

2. Mathematical model

In this work we focus our discussion on solving the convection-driven MHD dynamo problem in a rapidly rotating spherical shell with pseudo-vacuum magnetic boundary conditions. The spherical shell, with outer radius r_o and inner radius r_i, is filled with electrically conducting viscous incompressible fluids and rotates with a constant angular velocity $\mathbf{\Omega} = \Omega\hat{z}$, where $\hat{z}$ is a unit vector parallel to the axis of rotation. The incompressible fluids in the spherical shell is assumed to satisfy the Boussinesq approximation, with the density ρ, kinetic viscosity ν, thermal diffusivity κ, thermal expand coefficiency α, magnetic diffusivity η, magnetic permeability μ. The temperatures on the inner and outer boundaries are fixed to be T_i and T_o, respectively and the temperature difference is denoted by $\Delta T = T_i - T_o$. Choosing the shell thickness $D = r_o - r_i$ as the fundamental length scale, D^2/ν as the time scale, ν/D as the velocity scale, ΔT as the temperature scale, $\sqrt{\rho\mu\eta\Omega}$ as the magnetic field scale, $\rho\nu\Omega$ as the pressure scale, we can obtain the non-dimensional governing equations of the MHD dynamo problem

$$E\left(\frac{\partial \mathbf{u}}{\partial t} + \mathbf{u}\cdot\nabla\mathbf{u} - \nabla^2\mathbf{u}\right) + 2\hat{z}\times\mathbf{u} + \nabla P = Ra\frac{\mathbf{r}}{r_o}\left(T - T_0\right) + \frac{1}{Pm}\mathbf{B}\cdot\nabla\mathbf{B},$$

$$(1)$$

$$\nabla\cdot\mathbf{u} = 0, \tag{2}$$

$$\frac{\partial T}{\partial t} + \mathbf{u}\cdot\nabla T = \frac{1}{Pr}\nabla^2 T, \tag{3}$$

$$\frac{\partial \mathbf{B}}{\partial t} = \nabla\times(\mathbf{u}\times\mathbf{B}) + \frac{1}{Pm}\nabla^2\mathbf{B}, \tag{4}$$

$$\nabla\cdot\mathbf{B} = 0, \tag{5}$$

where $\mathbf{u}$, P, $\mathbf{B}$, T, T_0 and $\mathbf{r}$ are non-dimensional velocity, reduced pressure, magnetic field, temperature, reference temperature and spatial position vector, respectively. The reference temperature T_0 can be expressed by

$$T_0(r) = r_i\left(\frac{r_o}{r} - 1\right), \tag{6}$$

where the dimensionless radii are set to be $r_i = 7/13, r_o = 20/13$. The non-dimensional parameters E, Ra, Pr, Pm in the above equations are Ekman num-

ber, modified Rayleigh number, Prandtl number and magnetic Prandtl number respectively and defined by

$$E = \frac{\nu}{\Omega D^2}, \quad Ra = \frac{\alpha g_o \Delta T D}{\nu \Omega}, \quad Pr = \frac{\nu}{\kappa}, \quad Pm = \frac{\nu}{\eta}, \tag{7}$$

where g_o is the gravitational acceleration at the outer radius.

An equivalent form of the magnetic induction equation (4) is

$$\frac{\partial \mathbf{B}}{\partial t} = \nabla \times (\mathbf{u} \times \mathbf{B}) - \frac{1}{Pm} \nabla \times \nabla \times \mathbf{B}. \tag{8}$$

Applying the divergence operator to the above equation, we can obtain

$$\frac{\partial (\nabla \cdot \mathbf{B})}{\partial t} = 0. \tag{9}$$

This equation indicates that the magnetic field will keep the divergence-free constraint (5) all the time in the evolution if the initial magnetic field is solenoidal. In numerical simulations, however, the divergence-free constraint is difficult to maintain. To overcome this difficulty, we adopt a technique of introducing a pseudo-pressure gradient into the magnetic induction equation (Tóth, 2000; Harder and Hansen, 2005; Chan et al., 2007; Vantieghem et al., 2016) and replace the induction equation (4) with the following equation

$$\frac{\partial \mathbf{B}}{\partial t} + \frac{1}{E} \nabla P_b = \nabla \times (\mathbf{u} \times \mathbf{B}) + \frac{1}{Pm} \nabla^2 \mathbf{B}, \tag{10}$$

where P_b is the pseudo-pressure. Therefore, a projection method similar to the well-known treatment (Chorin, 1968; Guermond et al., 2006) of velocity fields can be applied to the magnetic field to ensure the divergence-free constraint.

Replacing the temperature T with an auxiliary temperature variable $\Theta = T - T_0$, we can rewrite the non-dimensional governing equations as

$$\frac{\partial \mathbf{u}}{\partial t} - \nabla^2 \mathbf{u} + \frac{2}{E} \hat{z} \times \mathbf{u} - \frac{Ra}{E r_o} \Theta \mathbf{r} + \frac{1}{E} \nabla P = -\mathbf{u} \cdot \nabla \mathbf{u} + \frac{1}{EPm} \mathbf{B} \cdot \nabla \mathbf{B}, \tag{11}$$

$$\frac{\partial \Theta}{\partial t} - \frac{1}{Pr} \nabla^2 \Theta - \frac{r_i r_o}{r^3} \mathbf{u} \cdot \mathbf{r} = -\mathbf{u} \cdot \nabla \Theta, \tag{12}$$

$$\frac{\partial \mathbf{B}}{\partial t} - \frac{1}{Pm} \nabla^2 \mathbf{B} + \frac{1}{E} \nabla P_b = (\mathbf{B} \cdot \nabla) \mathbf{u} - (\mathbf{u} \cdot \nabla) \mathbf{B}, \tag{13}$$

$$\nabla \cdot \mathbf{u} = 0, \tag{14}$$

$$\nabla \cdot \mathbf{B} = 0. \tag{15}$$

To solve the above system, it is necessary to apply proper boundary conditions to the velocity, temperature and magnetic field. On the shell boundaries, we employ the no-slip condition for the velocity and isothermal condition for the temperature,

$$\mathbf{u} = 0, \quad \Theta = 0, \qquad r = r_i, r_o. \tag{16}$$

And for the magnetic field, we adopt the pseudo-vacuum boundary condition

$$\mathbf{r} \times \mathbf{B} = 0, \qquad r = r_i, r_o, \tag{17}$$

on the shell boundaries, which indicates that the tangential component of $\mathbf{B}$ is zero and only the normal component exists (Kageyama and Sato, 1995; Jackson et al., 2014). The value of the normal component on the boundaries can be constrained by the solenoidal condition $\nabla \cdot \mathbf{B} = 0$.

3. Numerical methods

In this section, we present the proposed numerical methods to discretize and solve the MHD dynamo equations (11)–(15) with the boundary conditions (16)–(17). Since some of the algorithms have already been introduced in a previous work that does not involve the magnetic field (Yin et al., 2017), we will focus on the treatments of the issues related to the magnetic field.

3.1. Temporal integration scheme

A second-order approximate factorization method (Dukowicz and Dvinsky, 1992) was applied successfully to deal with the temporal integration and ensure the solenoidal condition of the velocity in the non-magnetic convection problem (Chan et al., 2006; Yin et al., 2017). In this section, we inherit the approximate factorization method and extend it to the temporal integration of the magnetic field. The dynamo governing equations (11)–(15) can be rewritten in

8

the following operator form

$$\frac{\partial \mathbf{u}}{\partial t} - L_1(\mathbf{u}) - R_1(\Theta) + G(P) = \mathbf{f}_1, \tag{18}$$

$$\frac{\partial \Theta}{\partial t} - L_2(\Theta) - R_2(\mathbf{u}) = f_2, \tag{19}$$

$$\frac{\partial \mathbf{B}}{\partial t} - L_3(\mathbf{B}) + G(P_b) = \mathbf{f}_3, \tag{20}$$

$$D(\mathbf{u}) = 0, \tag{21}$$

$$D(\mathbf{B}) = 0, \tag{22}$$

where the L_1, R_1, G, L_2, R_2, L_3 and D are linear operators defined by

$$\begin{cases} L_1(\mathbf{u}) = \nabla^2 \mathbf{u} - \dfrac{2}{E}(\hat{z} \times \mathbf{u}), \quad R_1(\Theta) = \dfrac{Ra}{Er_o}(\Theta \mathbf{r}), \quad G(P) = \dfrac{1}{E}\nabla P, \\[2mm] L_2(\Theta) = \dfrac{1}{Pr}\nabla^2 \Theta, \quad R_2(\mathbf{u}) = \dfrac{r_i r_o}{r^3}\mathbf{u} \cdot \mathbf{r}, \quad L_3(\mathbf{B}) = \dfrac{1}{Pm}\nabla^2 \mathbf{B}, \\[2mm] G(P_b) = \dfrac{1}{E}\nabla P_b, \quad D(\mathbf{u}) = \nabla \cdot \mathbf{u}, \quad D(\mathbf{B}) = \nabla \cdot \mathbf{B}, \end{cases} \tag{23}$$

and the right hand sides are nonlinear terms

$$\begin{cases} \mathbf{f}_1 = -\mathbf{u} \cdot \nabla \mathbf{u} + \dfrac{1}{EPm}\mathbf{B} \cdot \nabla \mathbf{B}, \\[2mm] f_2 = -\mathbf{u} \cdot \nabla \Theta, \\[2mm] \mathbf{f}_3 = \mathbf{B} \cdot \nabla \mathbf{u} - \mathbf{u} \cdot \nabla \mathbf{B}. \end{cases} \tag{24}$$

Applying the Crank-Nicolson scheme to the linear operators and discretizing all terms spatially, the governing equations (18)–(22) can be fully discretized as

$$\frac{\mathbf{u}^{n+1} - \mathbf{u}^n}{\Delta t} - \mathcal{L}_1\left(\frac{\mathbf{u}^{n+1} + \mathbf{u}^n}{2}\right) - \mathcal{R}_1\left(\frac{\Theta^{n+1} + \Theta^n}{2}\right) + \mathcal{G}\left(\frac{P^{n+1} + P^n}{2}\right)$$
$$= \hat{\mathbf{f}}_1^{n+\frac{1}{2}} + O\left(\Delta t^2\right), \tag{25}$$

$$\frac{\Theta^{n+1} - \Theta^n}{\Delta t} - \mathcal{L}_2\left(\frac{\Theta^{n+1} + \Theta^n}{2}\right) - \mathcal{R}_2\left(\frac{\mathbf{u}^{n+1} + \mathbf{u}^n}{2}\right)$$
$$= \hat{f}_2^{n+\frac{1}{2}} + O\left(\Delta t^2\right), \tag{26}$$

$$\frac{\mathbf{B}^{n+1} - \mathbf{B}^n}{\Delta t} - \mathcal{L}_3\left(\frac{\mathbf{B}^{n+1} + \mathbf{B}^n}{2}\right) + \mathcal{G}\left(\frac{P_b^{n+1} + P_b^n}{2}\right)$$
$$= \hat{\mathbf{f}}_3^{n+\frac{1}{2}} + O\left(\Delta t^2\right), \tag{27}$$

$$\mathcal{D}\left(\mathbf{u}^{n+1}\right) = \mathcal{D}\left(\mathbf{B}^{n+1}\right) = 0, \tag{28}$$

9

where Δt is the time step size and n denotes the time step number. $\mathcal{L}_1$, $\mathcal{R}_1$, $\mathcal{G}$, $\mathcal{L}_2$, $\mathcal{R}_2$, $\mathcal{L}_3$ and $\mathcal{D}$ are discrete linear operators corresponding to the linear terms in equation (23). $\hat{\mathbf{f}}_1$, $\hat{f}_2$ and $\hat{\mathbf{f}}_3$ are the discrete nonlinear terms corresponding to equation (24). The nonlinear terms $\hat{\mathbf{f}}_1$, $\hat{f}_2$ and $\hat{\mathbf{f}}_3$ are calculated by the second-order Adams-Bashforth formula

$$f^{n+\frac{1}{2}} = \frac{3}{2}f^n - \frac{1}{2}f^{n-1} + O\left(\Delta t^2\right), \tag{29}$$

except the first time step by a first-order approximation $f^{\frac{1}{2}} = f^0$. The spatial discretization schemes of the linear and nonlinear terms in the above equations will be described in Section 3.2.

Moving the unknown terms about the time step $n+1$ to the left hand sides and others to the right, the equations (25)–(27) can be transformed into the following form

$$\tilde{\mathbf{u}}^{n+1} - \frac{\Delta t}{2}\mathcal{L}_1\left(\tilde{\mathbf{u}}^{n+1}\right) - \frac{\Delta t}{2}\mathcal{R}_1\left(\Theta^{n+1}\right) = \hat{\mathbf{u}}^n + \frac{\Delta t}{2}\mathcal{L}_1\left(\hat{\mathbf{u}}^n\right) + \frac{\Delta t}{2}\mathcal{R}_1\left(\Theta^n\right)$$
$$+ \Delta t\hat{\mathbf{f}}_1^{n+\frac{1}{2}} - \frac{\Delta t^2}{4}\mathcal{L}_1\mathcal{G}\left(P^{n+1} - P^n\right) + O\left(\Delta t^3\right), \tag{30}$$

$$\Theta^{n+1} - \frac{\Delta t}{2}\mathcal{L}_2\left(\Theta^{n+1}\right) - \frac{\Delta t}{2}\mathcal{R}_2\left(\tilde{\mathbf{u}}^{n+1}\right) = \Theta^n + \frac{\Delta t}{2}\mathcal{L}_2\left(\Theta^n\right) + \frac{\Delta t}{2}\mathcal{R}_2\left(\hat{\mathbf{u}}^n\right)$$
$$+ \Delta t\hat{f}_2^{n+\frac{1}{2}} - \frac{\Delta t^2}{4}\mathcal{R}_2\mathcal{G}\left(P^{n+1} - P^n\right) + O\left(\Delta t^3\right), \tag{31}$$

$$\tilde{\mathbf{B}}^{n+1} - \frac{\Delta t}{2}\mathcal{L}_3\left(\tilde{\mathbf{B}}^{n+1}\right) = \hat{\mathbf{B}}^n + \frac{\Delta t}{2}\mathcal{L}_3\left(\hat{\mathbf{B}}^n\right)$$
$$+ \Delta t\hat{\mathbf{f}}_3^{n+\frac{1}{2}} - \frac{\Delta t^2}{4}\mathcal{L}_3\mathcal{G}\left(P_b^{n+1} - P_b^n\right) + O\left(\Delta t^3\right), \tag{32}$$

where $\tilde{\mathbf{u}}^{n+1}$, $\hat{\mathbf{u}}^n$, $\tilde{\mathbf{B}}^{n+1}$ and $\hat{\mathbf{B}}^n$ are intermediate velocities and magnetic fields defined by

$$\tilde{\mathbf{u}}^{n+1} = \mathbf{u}^{n+1} + \frac{\Delta t}{2}\mathcal{G}\left(P^{n+1}\right), \quad \tilde{\mathbf{B}}^{n+1} = \mathbf{B}^{n+1} + \frac{\Delta t}{2}\mathcal{G}\left(P_b^{n+1}\right), \tag{33}$$

$$\hat{\mathbf{u}}^n = \mathbf{u}^n - \frac{\Delta t}{2}\mathcal{G}\left(P^n\right), \quad \hat{\mathbf{B}}^n = \mathbf{B}^n - \frac{\Delta t}{2}\mathcal{G}\left(P_b^n\right). \tag{34}$$

By expanding P^{n+1} in Taylor series about P^n, It can be observed that the pressure terms $(-\Delta t^2/4)\mathcal{L}_1\mathcal{G}(P^{n+1} - P^n)$, $(-\Delta t^2/4)\mathcal{R}_2\mathcal{G}(P^{n+1} - P^n)$ and $(-\Delta t^2/4)\mathcal{L}_3\mathcal{G}(P_b^{n+1} - P_b^n)$ are all of $O(\Delta t^3)$. Discarding these terms as well

10

as the temporal truncation error, we can obtain the following fully discretized time stepping equations for the intermediate velocity $\tilde{\mathbf{u}}^{n+1}$, temperature Θ and intermediate magnetic field $\tilde{\mathbf{B}}^{n+1}$

$$
\tilde{\mathbf{u}}^{n+1} - \frac{\Delta t}{2}\mathcal{L}_1\left(\tilde{\mathbf{u}}^{n+1}\right) - \frac{\Delta t}{2}\mathcal{R}_1\left(\Theta^{n+1}\right) = \hat{\mathbf{u}}^n + \frac{\Delta t}{2}\mathcal{L}_1\left(\hat{\mathbf{u}}^n\right) + \frac{\Delta t}{2}\mathcal{R}_1\left(\Theta^n\right)
$$
$$
+ \Delta t\hat{\mathbf{f}}_1^{n+\frac{1}{2}}, \tag{35}
$$
$$
\Theta^{n+1} - \frac{\Delta t}{2}\mathcal{L}_2\left(\Theta^{n+1}\right) - \frac{\Delta t}{2}\mathcal{R}_2\left(\tilde{\mathbf{u}}^{n+1}\right) = \Theta^n + \frac{\Delta t}{2}\mathcal{L}_2\left(\Theta^n\right) + \frac{\Delta t}{2}\mathcal{R}_2\left(\hat{\mathbf{u}}^n\right)
$$
$$
+ \Delta t\hat{f}_2^{n+\frac{1}{2}}, \tag{36}
$$
$$
\tilde{\mathbf{B}}^{n+1} - \frac{\Delta t}{2}\mathcal{L}_3\left(\tilde{\mathbf{B}}^{n+1}\right) = \hat{\mathbf{B}}^n + \frac{\Delta t}{2}\mathcal{L}_3\left(\hat{\mathbf{B}}^n\right) + \Delta t\hat{\mathbf{f}}_3^{n+\frac{1}{2}}. \tag{37}
$$

Applying the divergence operator to equation (33) and subtracting equation (28), we can obtain two Poisson equations for the pressure P^{n+1} and pseudo-pressure P_b^{n+1} respectively

$$
\frac{\Delta t}{2}\mathcal{D}\mathcal{G}\left(P^{n+1}\right) = \mathcal{D}\left(\tilde{\mathbf{u}}^{n+1}\right), \tag{38}
$$
$$
\frac{\Delta t}{2}\mathcal{D}\mathcal{G}\left(P_b^{n+1}\right) = \mathcal{D}\left(\tilde{\mathbf{B}}^{n+1}\right). \tag{39}
$$

Boundary conditions for the pressure P and pseudo-pressure P_b are required to solve the above equations. The Neumann boundary condition $\mathbf{n} \cdot \nabla P = 0$ is applied to the pressure P, where $\mathbf{n}$ denotes the outward normal unit vector, and a detailed discussion can be found in Yin et al. (2017). The pseudo-vacuum condition (17) is applied to both P and P_b, and according to equation (33), we can obtain $\mathbf{n} \times \nabla P_b = 0$, which indicates a Dirichlet boundary condition of P_b on the boundaries.

As a result, two linear algebraic systems are obtained including the equations for the velocity, temperature and magnetic field (VTBE) (35)–(37) and the equations for the pressure and pseudo-pressure (PPBE) (38)–(39). Based on these two linear systems, a predictor-corrector procedure is adopted to obtain the required numerical solutions. The outline of the resulting semi-implicit time stepping scheme can be summarized as follows:

Step 1: According to the previous values $\mathbf{u}^n$, Θ^n, $\mathbf{B}^n$ and P^n, calculate $\hat{\mathbf{u}}^n$

and $\hat{\mathbf{B}}^n$ and then solve VTBE to obtain the current solutions $\tilde{\mathbf{u}}^{n+1}$, Θ^{n+1} and $\tilde{\mathbf{B}}^{n+1}$.

Step 2: Solve PPBE to obtain P^{n+1} and P_b^{n+1} based on $\tilde{\mathbf{u}}^{n+1}$ and $\tilde{\mathbf{B}}^{n+1}$.

Step 3: Update the current solutions $\mathbf{u}^{n+1}$ and $\mathbf{B}^{n+1}$ according to equation (33).

In the above time stepping scheme, the intermediate variables $\hat{\mathbf{u}}^n$ and $\hat{\mathbf{B}}^n$ are calculated from equations (34) except the initial values $\hat{\mathbf{u}}^0$ and $\hat{\mathbf{B}}^0$ by first-order approximations $\hat{\mathbf{u}}^0 = \mathbf{u}^0$, $\hat{\mathbf{B}}^0 = \mathbf{B}^0$.

3.2. Finite volume spatial discretization

As an alternative to the traditional latitude-longitude grid that suffers from disadvantages such as singularity and non-uniformity, the cubed-sphere grid (Sadourny, 1972; Ronchi et al., 1996) obtained by a projection of the inscribed cube is becoming popular for problems defined on the spherical geometry. Adopting the cubed-sphere grid based on the equiangular gnomonic projection (Ronchi et al., 1996), a spherical shell is divided into six identical blocks, of which each block is described by a local coordinate system (ξ, η, r), $\xi, \eta \in [-\pi/4, \pi/4]$. With each block being divided uniformly in the three coordinate directions, a quasi-uniform cubed-sphere grid covering the whole spherical shell can be obtained, as shown in Fig. 1. In spite of the complexity caused by the non-orthogonality of ξ and η, the resulting cubed-sphere grid is quite regular and thus can be adapted well to the algorithms of domain decomposition (Toselli and Widlund, 2005) and multigrid (Saad, 2003).

A collocated arrangement by which all the unknown variables $(\mathbf{u}, \Theta, \mathbf{B}, P, P_b)$ are located at the center of grid cells is employed in the spatial discretization. For each block, the numbers of grid cells in ξ and η directions are set to be the same value N_s and the cell number in r direction is denoted by N_r. The coordinates of the unknown point with the indices $(i, j, k), 0 \leq i, j \leq N_s - 1, 0 \leq k \leq N_r - 1$ in each block can be calculated by

$$\xi_i = -\frac{\pi}{4} + (i + 0.5)h_s, \quad \eta_j = -\frac{\pi}{4} + (j + 0.5)h_s, \quad r_k = r_i + (k + 0.5)h_r, \quad (40)$$
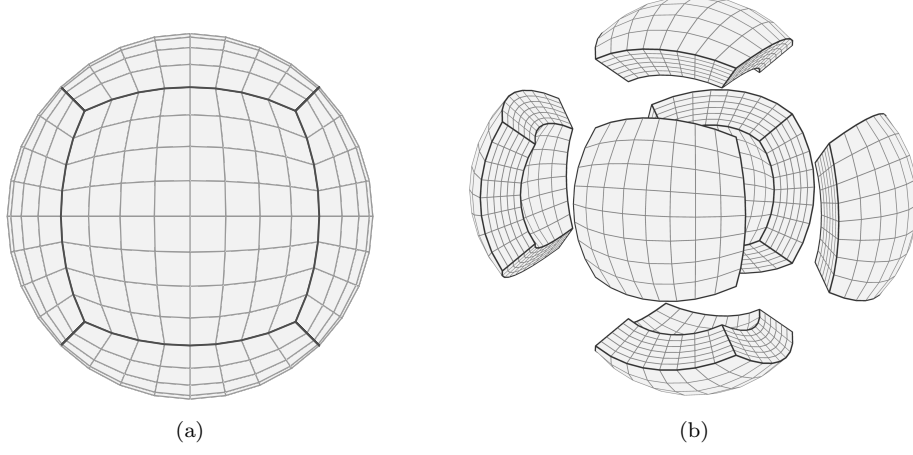
Figure 1: A cubed-sphere grid based on the equiangular gnomonic projection. (a) (ξ, η) grid on a spherical surface, (b) An open grid by shifting the six blocks outwards.

where $h_s = \pi/(2N_s)$, $h_r = (r_o - r_i)/N_r$ are the grid spacings in ξ (η) and r directions, respectively. The total cell number of the cubed-sphere grid is denoted by $N = N_s \times N_s \times N_r \times 6$.

A finite volume scheme based on the cubed-sphere grid is applied to the spatial discretization of the linear operators in (23) and the nonlinear terms in (24). Given a vector $\mathbf{v}$, its divergence at the center of the grid cell (i, j, k) is numerically approximated by the Gauss theorem

$$
\begin{aligned}
\nabla \cdot \mathbf{v}|_{i,j,k} &\approx \frac{1}{V_{i,j,k}} \int_V \nabla \cdot \mathbf{v} \, \mathrm{d}V = \frac{1}{V_{i,j,k}} \oint_S \mathbf{v} \cdot \mathrm{d}\mathbf{S} \\
&\approx \frac{1}{V_{i,j,k}} \Big[\left(v^1 \sqrt{g}\right)_{i+\frac{1}{2},j,k} h_s h_r - \left(v^1 \sqrt{g}\right)_{i-\frac{1}{2},j,k} h_s h_r \\
&\quad + \left(v^2 \sqrt{g}\right)_{i,j+\frac{1}{2},k} h_s h_r - \left(v^2 \sqrt{g}\right)_{i,j-\frac{1}{2},k} h_s h_r \\
&\quad + \left(v^3 \sqrt{g}\right)_{i,j,k+\frac{1}{2}} h_s h_s - \left(v^3 \sqrt{g}\right)_{i,j,k-\frac{1}{2}} h_s h_s \Big],
\end{aligned}
\tag{41}
$$

where $V_{i,j,k} \approx \sqrt{g}_{i,j,k} h_s h_s h_r$ refers to the volume of the grid cell (i, j, k), (v^1, v^2, v^3) are the contravariant components of $\mathbf{v}$ and g is the determinant of the covariant components g_{mn} of the metric tensor in the cubed-sphere grid

$$
\sqrt{g} = \sqrt{\det(g_{mn})} = r^2 \sec^2 \xi \sec^2 \eta / \left(1 + \tan^2 \xi + \tan^2 \eta\right)^{\frac{3}{2}}.
\tag{42}
$$

13

The spatial differential operators in equations (23) and (24) are transformed into the divergence forms and then discretized according to equation (41).

Most of the spatial terms in the governing equations (18)–(22) have been discussed in our previous work (Yin et al., 2017). In this section, we focus on the new terms related to the magnetic field $\mathbf{B}$, including the Laplacian term $\nabla^2\mathbf{B}$, divergence term $\nabla \cdot \mathbf{B}$ and nonlinear terms $\mathbf{B} \cdot \nabla\mathbf{B}$, $\mathbf{B} \cdot \nabla\mathbf{u}$ and $\mathbf{u} \cdot \nabla\mathbf{B}$. The Laplacian term $\nabla^2\mathbf{B}$ and divergence term $\nabla \cdot \mathbf{B}$ are discretized in the same way as $\nabla^2\mathbf{u}$ and $\nabla \cdot \mathbf{u}$, respectively, while some additional effort is required for the three nonlinear terms.

To deal with the three nonlinear terms in a uniform way, we consider a generic form $\mathbf{a} \cdot \nabla\mathbf{b}$, where $\mathbf{a}$ and $\mathbf{b}$ are two arbitrary vectors conforming divergence-free condition $\nabla \cdot \mathbf{a} = \nabla \cdot \mathbf{b} = 0$. The nonlinear term $\mathbf{a} \cdot \nabla\mathbf{b}$ can be rewritten in a conservative form and divided into two parts

$$\mathbf{a} \cdot \nabla\mathbf{b} = \nabla \cdot (\mathbf{a}\mathbf{b}) = \left[\nabla \cdot \left(\mathbf{a}b^k\right) + a^i b^j \Gamma_{ij}^k\right]\mathbf{g}_k, \quad i,j,k = 1,2,3, \qquad (43)$$

where $\Gamma_{ij}^k (i,j,k = 1,2,3)$ are the Christoffel symbols and $\mathbf{g}_k (k = 1,2,3)$ are the covariant base vectors in the cubed-sphere coordinate system. The divergence term is discretized in a finite volume scheme

$$\begin{aligned}
\nabla \cdot \left(\mathbf{a}b^k\right)\big|_{i,j,k} &\approx \frac{1}{V_{i,j,k}} \int_V \nabla \cdot \left(\mathbf{a}b^k\right) \, \mathrm{d}V = \frac{1}{V_{i,j,k}} \oint_S \left(\mathbf{a}b^k\right) \cdot \mathrm{d}\mathbf{S} \\
&\approx \frac{1}{V_{i,j,k}} \left[\left(a^1 b^k \sqrt{g}\right)_{i+\frac{1}{2},j,k} h_s h_r - \left(a^1 b^k \sqrt{g}\right)_{i-\frac{1}{2},j,k} h_s h_r \right. \\
&\quad + \left(a^2 b^k \sqrt{g}\right)_{i,j+\frac{1}{2},k} h_s h_r - \left(a^2 b^k \sqrt{g}\right)_{i,j-\frac{1}{2},k} h_s h_r \\
&\quad \left. + \left(a^3 b^k \sqrt{g}\right)_{i,j,k+\frac{1}{2}} h_s h_s - \left(a^3 b^k \sqrt{g}\right)_{i,j,k-\frac{1}{2}} h_s h_s\right]. \qquad (44)
\end{aligned}$$

The rest term can be expressed as

$$\begin{aligned}
a^i b^j \Gamma_{ij}^1 &= a^1 b^1 \Gamma_{11}^1 + a^1 b^2 \Gamma_{12}^1 + a^1 b^3 \Gamma_{13}^1 + a^2 b^1 \Gamma_{21}^1 + a^3 b^1 \Gamma_{31}^1, \\
a^i b^j \Gamma_{ij}^2 &= a^1 b^2 \Gamma_{12}^2 + a^2 b^1 \Gamma_{21}^2 + a^2 b^2 \Gamma_{22}^2 + a^2 b^3 \Gamma_{23}^2 + a^3 b^2 \Gamma_{32}^2, \qquad (45) \\
a^i b^j \Gamma_{ij}^3 &= a^1 b^1 \Gamma_{11}^3 + a^1 b^2 \Gamma_{12}^3 + a^2 b^1 \Gamma_{21}^3 + a^2 b^2 \Gamma_{22}^3,
\end{aligned}$$

and is treated as a source term. We apply the above finite volume scheme to the three nonlinear terms $\mathbf{B} \cdot \nabla\mathbf{B}$, $\mathbf{B} \cdot \nabla\mathbf{u}$ and $\mathbf{u} \cdot \nabla\mathbf{B}$.

Some special attention should be paid to the boundary condition of the magnetic field. Let (B^1, B^2, B^3) denote the contravariant components of the magnetic field in the cubed-sphere grid. According to the pseudo-vacuum boundary condition (17), we can deduce that the tangential components of the magnetic field equal zero on the boundaries, i.e. $B^1 = B^2 = 0$. The normal component B^3 can be constrained by the solenoidal condition $\nabla \cdot \mathbf{B} = 0$. In the cubed-sphere grid, the solenoidal condition can be expressed as

$$\nabla \cdot \mathbf{B} = \frac{\partial B^1}{\partial \xi} + \frac{\partial B^2}{\partial \eta} + \left(\Gamma_{11}^1 + \Gamma_{12}^2\right) B^1 + \left(\Gamma_{12}^1 + \Gamma_{22}^2\right) B^2 + \frac{1}{r^2} \frac{\partial}{\partial r} \left(r^2 B^3\right) = 0. \quad (46)$$

Due to $B^1 = B^2 = 0$, we can obtain

$$\frac{\partial}{\partial r} \left(r^2 B^3\right) = 0, \quad (47)$$

following which the normal component of magnetic field B^3 on the boundaries is calculated.

3.3. Parallel solution and multilevel preconditioner

At each time step, there are two linear algebraic equations, i.e. VTBE and PPBE, to be considered. The Krylov subspace iterative method combined with the preconditioning technology is employed to solve these linear systems in this paper. With preconditioning, a linear system, e.g. $Ax = b$, is replaced with a right preconditioned system

$$A'x' = b, \quad (48)$$

where $A' = AM^{-1}, x' = Mx$. Here the matrix M is generally called preconditioner. For any time step, x' is initialized as $x_0' = Mx_0$ where x_0 is usually set to be the solution of previous time step. Then the new preconditioned linear system (48) is solved by a restarted generalized minimum residual (GMRES) algorithm until the residual satisfies

$$\|A'x' - b\| \leq \max\{\varepsilon_a, \varepsilon_r \|A'x_0' - b\|\}, \quad (49)$$

where ε_a, ε_r are the absolute and relative convergence tolerances, respectively. And finally the present time step solution x can be obtained by $x = M^{-1}x'$.

15

When solving the linear system (48) by the Krylov subspace iterative method, the convergence rate strongly depends on the condition number of the coefficient matrix $A' = AM^{-1}$ (Demmel, 1997). If A' is well conditioned, that is, its condition number is sufficiently small, the iteration number of the Krylov subspace method can be dramatically reduced. This can be achieved by choosing an appropriate preconditioner M. A good choice of the preconditioner should also help improve the scalability of parallel computations on large-scale supercomputers. In other words, with the aid of a scalable preconditioner, the iteration number should remain a steady level as the number of processor cores increases. It is often problem-dependent to construct an efficient and scalable preconditioner. In present study, we design a parallel multi-level restricted additive Schwarz preconditioner based on domain decomposition and multigrid method.

The cubed-sphere grid is divided into six identical blocks and each block is decomposed into $p = p_1 p_2 p_3$ non-overlapping subdomains in a structured manner, where p_1, p_2, p_3 are numbers of subdivisions corresponding to three coordinate directions respectively. Each subdomain is assigned to one processor core and the number of processor cores corresponding to each block is p. Thus the total number of processor cores is $6p$ as well as the total number of subdomains. For each non-overlapping subdomain Ω_i, $i = 1, 2, \ldots, 6p$, we can obtain a corresponding larger overlapping subdomain Ω_i^δ by extending Ω_i with δ layers of mesh cells, as shown in Fig. 2a. The subdomains containing one or more block interfaces are extended to the adjacent mesh cells of the neighbouring block(s). The extending parts of overlapping subdomains lead to data exchanges, i.e. communications between corresponding processor cores. To achieve good scalability, the influence of communication time should be reduced as much as possible.

Let N denote the total number of mesh cells and d be the number of degrees of freedom per point. Moreover, the number of mesh cells in overlapping subdomain Ω_i^δ is denoted by N_i^δ. Then we can define a one-level restricted additive
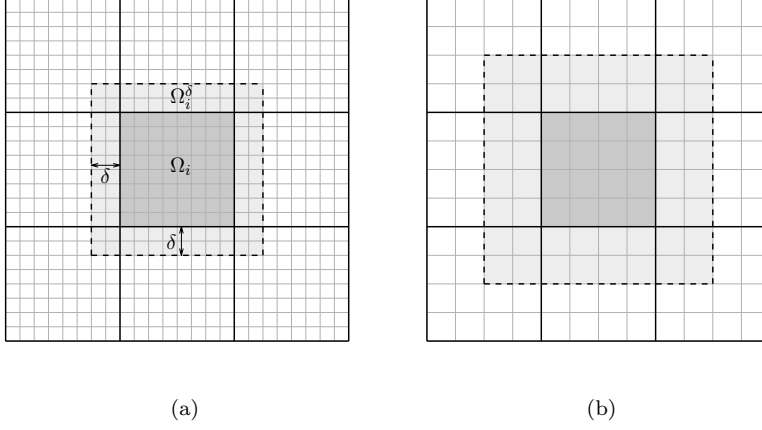
Figure 2: A two-dimensional illustration of domain decomposition and multigrid. (a) fine mesh, (b) coarse mesh of which the cell number in each direction is reduced by 1/2.

Schwarz (RAS) (Cai and Sarkis, 1999) preconditioner as

$$M_{\text{one}}^{-1} = \sum_{i=1}^{6p} \left(R_i^0\right)^{\text{T}} \left(A_i^\delta\right)^{-1} R_i^\delta. \tag{50}$$

The restriction operator R_i^δ is an $N_i^\delta \times N$ block matrix and its multiplication by a $N \times 1$ block vector defined on the entire domain results in a smaller $N_i^\delta \times 1$ block vector defined on the subdomain Ω_i^δ by dropping the components corresponding to the mesh cells outside Ω_i^δ. The element of the restriction matrix $\left(R_i^\delta\right)_{q_1,q_2}$, which is a $d \times d$ block submatrix, is an identity block if the integer indices $1 \leq q_1 \leq N_i^\delta$ and $1 \leq q_2 \leq N$ belong to a cell in the overlapping subdomain Ω_i^δ, or a block of zeros otherwise. As a special case, R_i^0 is also an $N_i^\delta \times N$ block matrix that is similarly defined, but is a restriction to the non-overlapping subdomain Ω_i. The matrix A_i^δ is the restriction of the coefficient matrix A to the overlapping subdomain Ω_i^δ with size $N_i^\delta \times N_i^\delta$ and is defined as $A_i^\delta = R_i^\delta A \left(R_i^\delta\right)^{\text{T}}$. The matrix-vector multiplication with $\left(A_i^\delta\right)^{-1}$ refers to solving a local linear system in subdomain Ω_i^δ and can be computed exactly by using a sparse LU factorization. Since LU factorization is often expensive and to form an exact preconditioner is generally not necessary, the matrix-vector multiplication

17

is usually obtained approximately by a less expensive incomplete LU (ILU) factorization.

In our previous work (Yin et al., 2017), it is found that the one-level RAS preconditioner can achieve very good parallel performance for the solution of the velocity-related equation but scales poorly for the pressure-related equation. To improve the scalability of the one-level RAS preconditioner, we employ a multi-level RAS method based on hybrid preconditioning (Mandel, 1994) and multigrid technique. By combining the one-level RAS preconditioner B_f with a coarse level preconditioner B_c defined on a coarser mesh in a multiplicative manner, we obtain a hybrid preconditioner

$$M_{\text{two}}^{-1} = \text{hybrid}\,(B_c, B_f) = B_c + B_f - B_f A_f B_c, \tag{51}$$

where $B_c = \mathcal{I}_c^f A_c^{-1} \mathcal{I}_f^c$ and A_f, A_c denote the coefficient matrices on the fine and coarse meshes, respectively. Here, $\mathcal{I}_f^c$ is a restriction operator mapping from a vector defined on the fine mesh to a coarse mesh vector. Similarly, $\mathcal{I}_c^f$ is a prolongation operator from the coarse mesh to the fine mesh. More precisely speaking, to calculate the multiplication of the hybrid two-level preconditioner and a vector x, $y = M_{\text{two}}^{-1} x$, we first apply a coarse mesh preconditioning

$$w = \left(\mathcal{I}_c^f A_c^{-1} \mathcal{I}_f^c\right) x, \tag{52}$$

and then correct the coarse solution by adding the fine mesh solution to obtain the final result

$$y = w + M_{\text{one}}^{-1}\left(x - A_f w\right). \tag{53}$$

For each application of the two-level preconditioner (51), a smaller linear system with the coefficient matrix A_c on the coarse mesh needs to be dealt with during the coarse mesh preconditioning. This coarse level linear system is solved by using preconditioned GMRES with a relative tolerance η_c. The coarse level preconditioner can be either one-level (50) or two-level (51). When a two-level preconditioner is adopted on the coarse mesh as well, another coarser mesh is required to form this preconditioner. Repeating the application of the two-level

RAS preconditioner (51) in multiple mesh levels can result in a multilevel hybrid RAS method.

The best choices for some of the options in the multilevel RAS preconditioner are often problem-dependent (Yang and Cai, 2011). One important option is the number of mesh levels, whose choice strongly depends on a specific circumstance. Since additional computational costs can be introduced by the coarse meshes, excessive mesh levels may lead to the degradation of computational efficiency. Furthermore, the choice of the number of mesh levels has a close relationship to the problem size. If too many mesh levels are applied when the problem size is not large enough, the computational load of each processor core may be too small. At this situation, the influence of communication time may become remarkable and the scalability may become worse. In the present study, we choose a two-level version with a coarse-to-fine mesh ratio 1:2 in each direction (see Fig. 2), by which an optimal efficiency is achieved in the considered spatial resolutions. If a larger resolution is required, three or more levels may be taken into consideration to achieve better performance. On the fine level mesh denoted by N, the preconditioner is

$$M_N^{-1} = \text{hybrid}\left(\mathcal{I}_{N/2}^N A_{N/2}^{-1} \mathcal{I}_N^{N/2}, \sum_{i=1}^{6p} \left((R_N)_i^0\right)^{\text{T}} \left((A_N)_i^\delta\right)^{-1} (R_N)_i^\delta\right), \qquad (54)$$

where $N/2$ refers to the coarse level mesh. A linear average restriction operator $\mathcal{I}_N^{N/2}$ and a piecewise constant interpolation operator $\mathcal{I}_{N/2}^N$ are employed due to their simplicities. The linear system about $A_{N/2}$ on the coarse level mesh is solved by an inner GMRES, preconditioned by a one-level RAS approach on the corresponding coarse level

$$M_{N/2}^{-1} = \sum_{i=1}^{6p} \left((R_{N/2})_i^0\right)^{\text{T}} \left((A_{N/2})_i^\delta\right)^{-1} (R_{N/2})_i^\delta. \qquad (55)$$

The choice of the subdomain solver at each level has a strong influence on the overall performance of the preconditioner. A large number of numerical experiments are often necessary to find out the proper selection. According to our tests, the ILU factorization with no fill-in, ILU(0), is chosen as the

subdomain solver for both the fine level $\left((A_N)_i^\delta\right)^{-1}$ in equation (54) and the coarse level $\left((A_{N/2})_i^\delta\right)^{-1}$ in equation (55).

4. Numerical results

We build the parallel simulation code based on the Portable, Extensible Toolkit for Scientific Computation (PETSc) library (Balay et al., 2013) and carry out the numerical experiments on the Sunway TaihuLight supercomputer (Fu et al., 2016) which took the top place of the Top-500 list (TOP500, 2020) as of June 2016. The two resulting sparse linear algebraic equations, i.e. VTBE and PPBE, are solved by GMRES algorithm with the restarting parameter 30. The absolute and relative tolerance of GMRES are respectively set to be 10^{-10}, 10^{-8} for VTBE and 10^{-8}, 10^{-6} for PPBE.

4.1. Benchmark cases

Following the well-known benchmark study of Christensen et al. (2001) where the insulating boundary condition is considered, a shell dynamo benchmarking exercise with pseudo-vacuum boundary conditions was carried out by Jackson et al. (2014) for the first time. Under the parameter regime in their work,

$$E = 10^{-3}, \quad Pr = 1, \quad Ra = 100, \quad Pm = 5, \tag{56}$$

at least five magnetic diffusion times are required to reach the quasi-steady state from the suggested initial condition

$$
\begin{aligned}
\mathbf{u}^0 &= 0, \\
\Theta^0 &= \frac{21}{\sqrt{17920\pi}} \left(1 - 3x^2 + 3x^4 - x^6\right) \sin^4(\theta)\cos(4\phi), \quad x = 2r - r_i - r_o, \\
B_r^0 &= \frac{5}{8} \frac{9r^3 - 4[4 + 3(r_i + r_o)]r^2 + [4r_o + r_i(4 + 3r_o)]6r - 48r_i r_o}{r} \cos(\theta), \\
B_\theta^0 &= -\frac{15}{4} \frac{(r - r_i)(r - r_o)(3r - 4)}{r} \sin(\theta), \\
B_\phi^0 &= \frac{15}{8} \sin[\pi(r - r_i)]\sin(2\theta).
\end{aligned}
\tag{57}
$$

In the same spirit, Vantieghem et al. (2016) suggests a new benchmark case with the non-dimensional control parameter

$$E = 10^{-3}, \quad Pr = 1, \quad Ra = 100, \quad Pm = 8, \tag{58}$$

and the same initial condition for the dynamo validations with pseudo-vacuum boundary conditions. According to their numerical results, a quasi-steady solution can be reached within less than one magnetic diffusion time. In this section, we follow both these benchmark cases to validate the correctness of our finite volume code. For simplicity, we refer to the benchmark case proposed by Jackson et al. (2014) as case P5 and the case suggested by Vantieghem et al. (2016) as case P8.

The values of the magnetic energy, kinetic energy and some other quantities at the final quasi-steady state are compared with the reference solutions for the benchmark case P5 and P8. To compare with these benchmark results, we should calculate these quantities in the consistent dimension. For the purpose of consistency, the kinetic energy E_{kin} and magnetic energy E_{mag} are defined as follows

$$E_{\text{kin}} = \frac{Pm^2}{2} \int \mathbf{u}^2 \, \mathrm{d}V, \tag{59}$$

$$E_{\text{mag}} = \frac{Pm}{2E} \int \mathbf{B}^2 \, \mathrm{d}V. \tag{60}$$

And the velocity, temperature and magnetic field are calculated by transforming from the quantities in present dimension

$$T' = T, \tag{61}$$

$$\mathbf{u}' = \mathbf{u}Pm, \tag{62}$$

$$\mathbf{B}' = \mathbf{B}/\sqrt{2}. \tag{63}$$

Firstly, the benchmark case P5 is run by our finite volume code in three different spatial resolutions, G64 ($N_s = 64, N_r = 96$), G80 ($N_s = 80, N_r = 120$), and G96 ($N_s = 96, N_r = 144$) until $t = 25.6$, when the magnetic time measured in units of magnetic diffusion time is $t_m = t/Pm = 5.12$. The time step sizes
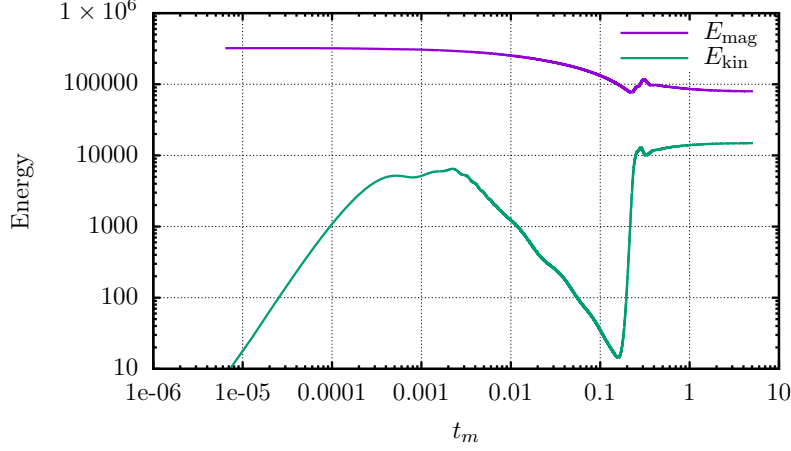
Figure 3: Time evolution of the magnetic energy E_{mag} and the kinematic energy E_{kin} on grid G96 for the benchmark case P5. The magnetic time t_m is measured in units of magnetic diffusion time $t_m = t/Pm$.

are $\Delta t = 4 \times 10^{-5}$ for both G64 and G80, and $\Delta t = 3.2 \times 10^{-5}$ for grid G96. The time evolution of the magnetic energy E_{mag} and the kinetic energy E_{kin} on grid G96 is displayed in Fig. 3, which shows good agreement with the result in Jackson et al. (2014).

From the quasi-steady solution, we calculate the final global data of the kinetic energy E_{kin}, magnetic energy E_{mag} and drift frequency ω, and the local data of T', u'_ϕ and B'_θ at a reference point in the equatorial plane at mid-depth where $u_r = 0$ and $(\partial u_r / \partial \phi) > 0$. The results are reported in Table 1, where comparisons with the recommended benchmark solution obtained by using spectral methods and three other results with local methods are also provided. V232 and ZS363 are respectively the largest resolution results obtained by the finite volume code V at the overall resolution $R = 232$ and the finite element code ZS at $R = 363$ reported in Jackson et al. (2014). And SFEMaNS refers to the finite element result reported in Matsui et al. (2016). The overall resolution R is defined as the third root of the number of degrees of freedom for each scalar variable $R = N_{\mathrm{grid}}^{1/3}$. The values in parentheses denote relative errors compared with the recommended benchmark solution obtained by spectral methods. From

22

Table 1: Comparison with the benchmark results for the case P5. G64, G80 and G96 are our numerical results in three different spatial resolutions. SM denotes the recommended benchmark solution (Jackson et al., 2014) obtained by the spectral methods. V232 and ZS363 are respectively the largest resolution results obtained by the finite volume code V at the overall resolution $R = 232$ and the finite element code ZS at $R = 363$ reported in Jackson et al. (2014). SFEMaNS refers to the finite element result reported in Matsui et al. (2016). The values in parentheses are relative errors compared with the SM results.

Results	E_{mag}	E_{kin}	T'	u'_ϕ	B'_θ	ω
G64	79503(0.71%)	14884(0.26%)	0.42590(0.002%)	-58.232(0.09%)	0.9936(0.06%)	3.5409(5.56%)
G80	79486(0.73%)	14878(0.22%)	0.42604(0.035%)	-58.149(0.05%)	0.9888(0.42%)	3.6781(1.90%)
G96	79686(0.48%)	14854(0.05%)	0.42593(0.009%)	-58.090(0.15%)	0.9901(0.29%)	3.7511(0.04%)
V232	79012(1.32%)	14941(0.64%)	0.42630(0.096%)	-57.932(0.42%)	0.9746(1.85%)	3.7457(0.10%)
ZS363	81210(1.42%)	15032(1.25%)	0.42700(0.261%)	-58.480(0.52%)	0.9951(0.21%)	3.7940(1.19%)
SFEMaNS	80578(0.63%)	14797(0.33%)	0.42553(0.085%)	-58.280(0.17%)	1.0015(0.86%)	
SM	80071	14846	0.42589	-58.179	0.9930	3.7495

Table 1, it is seen that the discrepancy is less than 1% for all quantities on all grids except the drift frequency ω at lower resolutions. Noticing that the overall resolution of the grid G64, G80 and G96 are respectively 133, 166 and 200, our finite volume code produces highly accurate solutions, which are comparable to and even better than the existing local results, for the benchmark case P5. In addition, the drift frequency ω shows good convergence rate as the spatial resolution increases.

The benchmark case P8 is then considered to further validate the proposed methods and the implemented finite volume code. An attractive advantage of this benchmark is that a quasi-steady solution can be reached within one magnetic diffusion time, which allows a much quicker validation in contrast to the benchmark case P5. It was found by Sheyko (2014) that two different types of dynamo solutions can be obtained when changing the initial magnetic field for this benchmark problem. For initial values of the magnetic energy between 407101 and 623428, such as the suggested one (57), one can obtain a quasi-steady solution expressed in the form $(\mathbf{u}, \mathbf{B}, \Theta) = f(r, \theta, \phi - \omega t)$. For the initial
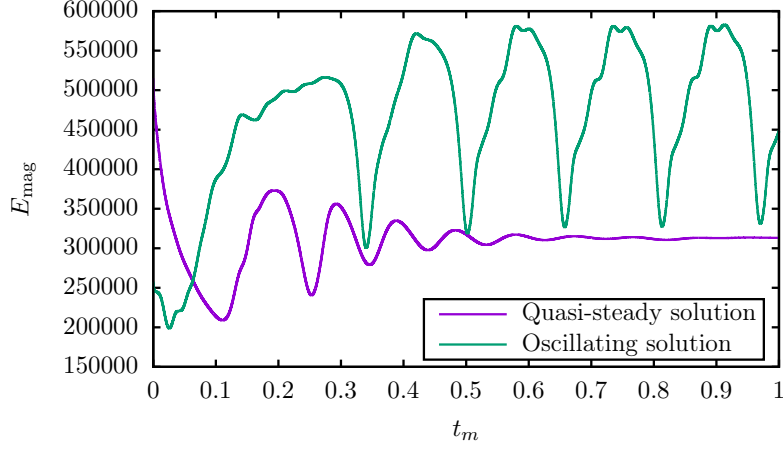
Figure 4: Time evolution of the magnetic energy E_{mag} on the grid G64 for the benchmark case P8 with two different initial magnetic field intensities. The magnetic time t_m is measured in units of magnetic diffusion time $t_m = t/Pm$.

magnetic energy outside this range, an oscillating dynamo solution can be found (Vantieghem et al., 2016).

The numerical tests of the case P8 are run on grid G64, G80 and G96 as well until $t = 8$, with the magnetic time $t_m = t/Pm = 1$. The time step sizes Δt corresponding to the grid G64, G80 and G96 are 5×10^{-5}, 5×10^{-5} and 4×10^{-5}, respectively. The time evolution of the magnetic energy E_{mag} on the grid G64 is displayed in Fig. 4, which also shows an oscillating solution obtained by decreasing the initial magnetic field $\mathbf{B}'_{\mathrm{initial}} = \mathbf{B}_{\mathrm{initial}}/\sqrt{2}$. We can see from the figure that the magnetic energy E_{mag} reaches a constant value within one magnetic diffusion time for the quasi-steady solution while the oscillating solution finally exhibits oscillation behaviour. The results of the time evolution in Fig. 4 are quite consistent with the benchmark (Vantieghem et al., 2016).

We calculate the reference quantities including E_{mag}, E_{kin}, T', u'_ϕ, B'_θ and ω from the final quasi-steady solution and summarize the comparison with the benchmark results in Table 2. The values in parentheses denote relative errors compared with the benchmark solution obtained by a pseudospectral method. It can be seen from Table 2 that our results are in good agreement with the

24

Table 2: Comparison with the benchmark results for the case P8. G64, G80 and G96 are our numerical results in three different spatial resolutions. FV64 and FV128 refer to the finite volume results in Vantieghem et al. (2016) with six blocks of 64^3 and 128^3 grid points, respectively. PS denotes the suggested benchmark solution (Vantieghem et al., 2016) obtained by the pseudospectral method. The values in parentheses are relative errors compared with the PS results.

Results	E_{mag}	E_{kin}	T'	u'_ϕ	B'_θ	ω
G64	313188.0(0.14%)	21762.6(0.59%)	0.3935(0.08%)	-80.64(0.36%)	2.2137(1.44%)	5.2215(6.07%)
G80	312799.0(0.01%)	21710.2(0.35%)	0.3934(0.05%)	-80.81(0.15%)	2.1977(0.71%)	5.3825(3.17%)
G96	312619.0(0.04%)	21686.1(0.24%)	0.3933(0.03%)	-80.88(0.06%)	2.1888(0.30%)	5.4827(1.37%)
FV64	309086.0(1.17%)	21502.1(0.61%)	0.3920(0.31%)	-81.23(0.36%)	2.1510(1.43%)	5.6453(1.55%)
FV128	311950.2(0.26%)	21576.2(0.27%)	0.3925(0.18%)	-80.74(0.24%)	2.1839(0.07%)	5.4959(1.13%)
PS	312754.7	21634.9	0.3932	-80.9318	2.1823	5.5588

benchmark pseudospectral solution and the accuracy is comparable to the existing finite volume results. Besides, the relative errors of the global and local quantities become smaller as the spatial resolution increases.

The spatial structure of the quasi-steady solution on the grid G96 is distinctly shown in Figs 5–7. Fig. 5 depicts the equatorial slices of the quasi-steady quantities including T', B'_θ, u'_ϕ and u'_r. It shows good agreement with the benchmark results (Vantieghem et al., 2016). Fig. 6 gives the contours on the mid-depth spherical surface of T', u'_r and B'_r, and Fig. 7 displays the contour of B'_r on the outer boundary surface. The spatial structure of the four-fold azimuthal symmetry can be observed from these figures.

4.2. Parallel performance

The parallel performances of the one-level and two-level RAS preconditioner are reported systematically in this section. In terms of the solver options, the overlap size is $\delta = 1$ and the subdomain solver is ILU(0) for the one-level RAS preconditioner. For the two-level method, the overlap size $\delta = 1$ and the subdomain solver ILU(0) are used for both the fine level and coarse level, while the relative tolerance of the inner GMRES on the coarse level is set to be 0.1. We
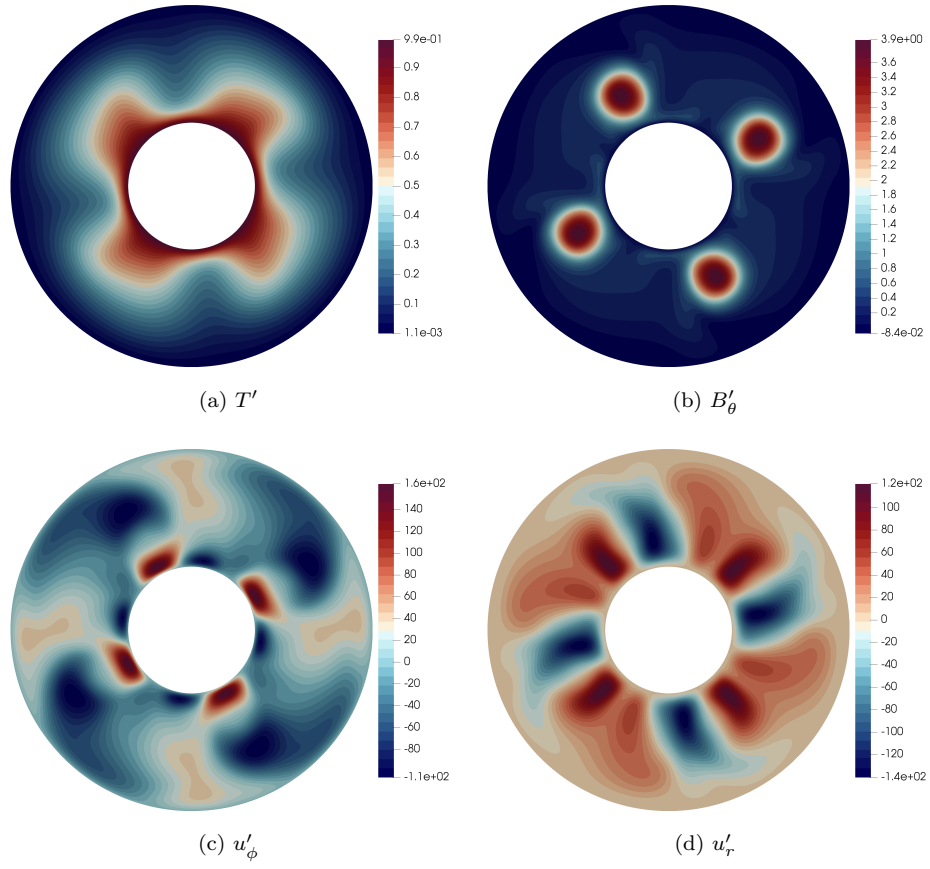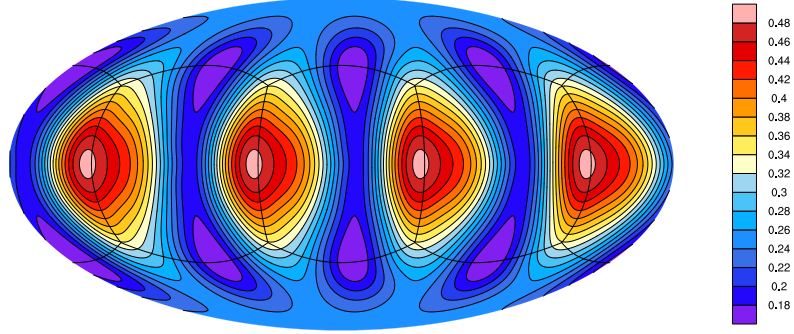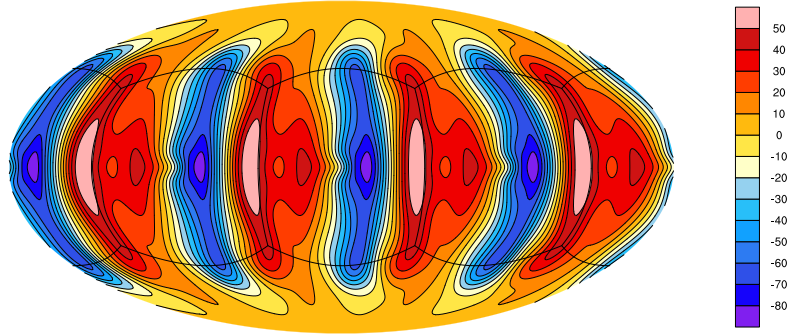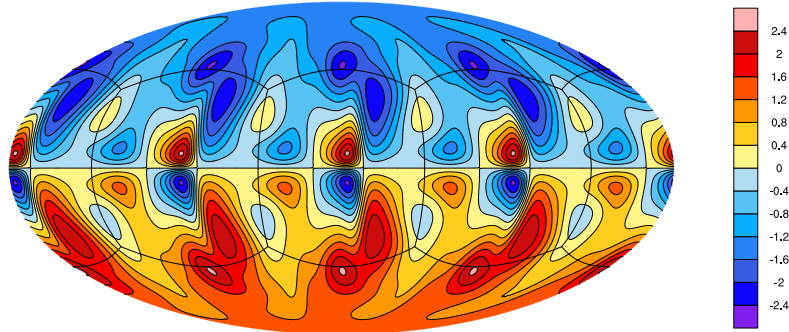
(a) T'

(b) B'_θ

(c) u'_ϕ

(d) u'_r

Figure 5: Equatorial slices of the quasi-steady solution on the grid G96 including T' (a), B'_θ (b), u'_ϕ (c) and u'_r (d).

(a) T'

(b) u'_r

(c) B'_r

Figure 6: Contours on the mid-depth spherical surface of the quasi-steady solution on the grid G96 including T' (a), u'_r (b) and B'_r (c). The block interfaces of the cubed-sphere grid are denoted by black lines.
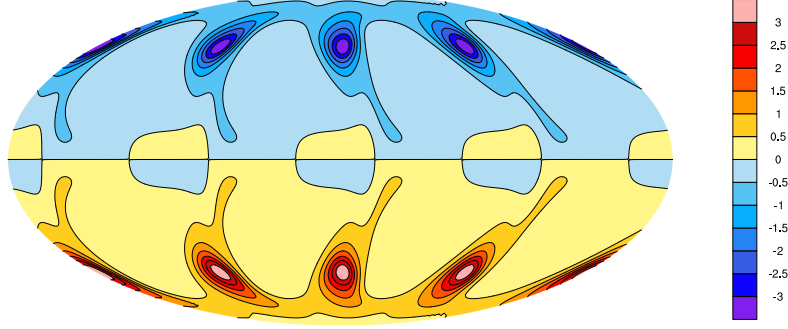
Figure 7: Contour of B'_r on the outer boundary surface of the quasi-steady solution on the grid G96.

apply both the one-level and two-level preconditioner to the solution of PPBE and compare the two results on efficiency and performance. The VTBE is only solved by GMRES with the one-level preconditioner.

Firstly, the strong scalability of the GMRES algorithm is studied with a fixed mesh $144 \times 144 \times 168 \times 6$ (about 20.9 million mesh cells) and a constant time step size $\Delta t = 1 \times 10^{-5}$. The strong scalability refers to the influence of the number of processor cores on the compute time for the problem with a fixed spatial resolution. In the ideal situation, the compute time should be reduced proportionally as the number of processor cores increases. We double the number of processor cores from 1296 up to 10368 and average the corresponding iteration number and compute time of GMRES over the first ten time steps. The averaged results are summarized in Table 3.

It is observed from Table 3 that the averaged iteration number of GMRES for VTBE remains unchanged as the number of processor cores increases from 1296 to 10368, and the iteration number of PPBE strongly depends on the employed preconditioner. For the one-level preconditioner, the iteration number of PPBE increases mildly as the number of processor cores is doubled. With the two-level preconditioner being employed, the iteration number of PPBE is dramatically reduced and is kept to a low level in spite of the double growth in the number of processor cores. In terms of the compute time of PPBE,

Table 3: Strong scaling results with a fixed mesh $144 \times 144 \times 168 \times 6$ and a constant time step size $\Delta t = 1 \times 10^{-5}$. The results are averaged over the first ten time steps. The averaged iteration numbers of the inner GMRES on the coarse mesh are given in parentheses when using the two-level RAS preconditioner. np denotes the number of processor cores.

| np | VTBE | | | PPBE | | | |
| | Iteration number | Compute time (s) | | Iteration number | | Compute time (s) | |
	one-level	one-level		one-level	two-level	one-level	two-level
1296	3.0	6.65		144.9	22.0(13.4)	29.69	15.80
2592	3.0	3.41		154.0	22.2(16.0)	16.90	10.18
5184	3.0	1.77		158.0	22.1(14.0)	9.60	5.72
10368	3.0	0.92		151.1	22.4(16.1)	5.24	4.20

the two-level preconditioner is about 20%–47% faster than the one-level, which indicates a noticeable improvement of computational efficiency. Fig. 8 displays the averaged compute time of VTBE and PPBE with respect to the number of processor cores. We can observe from the figure that the GMRES algorithm for VTBE scales very well with up to 10368 processor cores and its strong scalability is quite close to the ideal situation. The GMRES algorithm for PPBE scales well if the number of processor cores is not too large. When using a large number of processor cores, e.g. 10368, the strong scalability, as well as the efficiency improvement by the two-level preconditioner, degrade to some extent, because the amount of computations on each processor core is too small.

To further investigate the performance of the proposed algorithms, we test our code in terms of the weak scalability, which usually draws more interest in practical applications. The weak scalability focuses on the variation of the compute time with respect to the increase in the number of processor cores while the computational load on each processor core is fixed. The compute time should remain the same as the number of processor cores grows in the ideal situation. In our weak scaling test, the time step size is set to be $\Delta t = 1 \times 10^{-5}$ and the mesh size assigned to each processor core is fixed to $20 \times 20 \times 20$. The number of processor cores is doubled from 648 to 10368 and the corresponding spatial
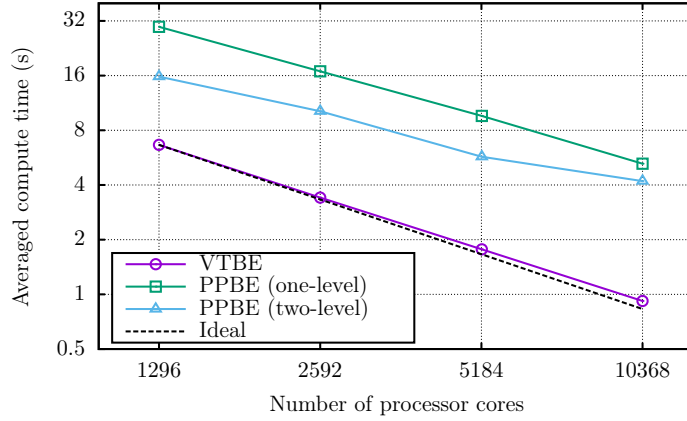
29

Figure 8: Strong scaling results displaying the averaged compute time of VTBE and PPBE with respect to the number of processor cores. The dash line refers to the ideal situation.

resolution is increased proportionally from $120 \times 120 \times 60 \times 6$ to $240 \times 240 \times 240 \times 6$ (about 82.9 million mesh cells). Table 4 displays the corresponding iteration number and compute time of GMRES for VTBE and PPBE averaged over the first ten time steps.

From Table 4, we can find that both the iteration number and the compute time of VTBE grow slowly with respect to the increase in the number of processor cores. The compute time only increases by 44%, as the number of processor cores increases from 648 to 10368 (16 times larger). For PPBE, the iteration number of the one-level preconditioner grows fast, while the iteration number of the two-level method stays at a low level. In terms of the compute time of PPBE, the increase of the one-level preconditioner is 139% from 648 to 10368 processor cores, which is much larger than 53% of the two-level method. In addition, the two-level preconditioner is about 32%–58% faster than the one-level as the number of processor cores doubles from 648 to 10368. The variation of the averaged compute time with respect to the number of processor cores is further displayed in Fig. 9. From the figure it can be seen that the VTBE and the PPBE with the two-level RAS preconditioner scales quite well while the PPBE with the one-level method scales a little worse in terms of the weak scalability.

Table 4: Weak scaling results with a fixed mesh $20 \times 20 \times 20$ for each processor core and a constant time step size $\Delta t = 1 \times 10^{-5}$. The results are averaged over the first ten time steps. The averaged iteration numbers of the inner GMRES on the coarse mesh are given in parentheses when using the two-level RAS preconditioner. np denotes the number of processor cores.

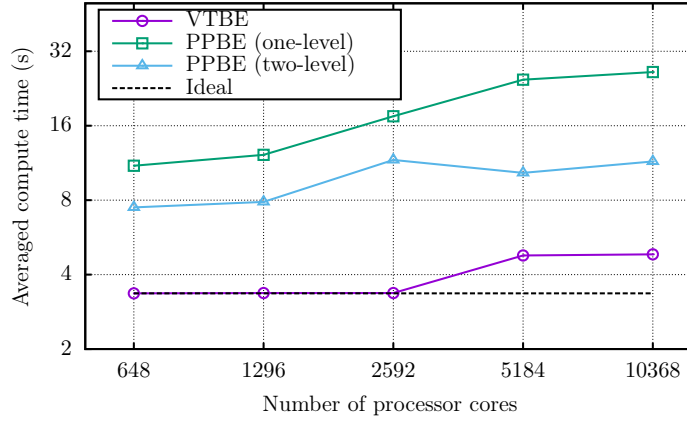| np | VTBE | | PPBE | | | |
	Iteration number	Compute time (s)	Iteration number		Compute time (s)	
	one-level	one-level	one-level	two-level	one-level	two-level
648	3.0	3.36	103.9	21.8(10.1)	11.02	7.48
1296	3.0	3.37	114.1	21.7(11.7)	12.20	7.87
2592	3.0	3.37	162.7	24.8(17.0)	17.47	11.63
5184	4.0	4.78	225.5	21.8(16.7)	24.56	10.31
10368	4.1	4.83	240.4	21.4(18.9)	26.37	11.47

Figure 9: Weak scaling results displaying the average compute time of VTBE and PPBE with respect to the number of processor cores. The dash line refers to the ideal situation.

31

5. Conclusions

A scalable parallel solver for the convection-driven magnetohydrodynamic dynamo problem in a rapidly rotating spherical shell with pseudo-vacuum magnetic boundary conditions is developed in this paper. A finite volume method on a collocated quasi-uniform cubed-sphere grid is employed for the spatial discretization of the spherical shell dynamo equations. In terms of the temporal integration, a second-order approximate factorization method, applied successfully to the non-magnetic thermal convection problem in our previous study (Yin et al., 2017), is extended to the dynamo governing equations, resulting in two linear algebraic systems, VTBE and PPBE, that are both solved by a preconditioned Krylov subspace iterative method. To improve the computational efficiency and parallel performance, we design a multi-level restricted additive Schwarz preconditioner based on domain decomposition and multigrid method. We perform the simulations of two benchmark cases suggested respectively by Jackson et al. (2014) and Vantieghem et al. (2016) and obtain highly accurate numerical solutions, comparable to the existing local method results reported in (Jackson et al., 2014; Vantieghem et al., 2016; Matsui et al., 2016). Several numerical tests are carried out to investigate the computational efficiency and the parallel performance with up to 10368 processor cores on the Sunway Taihu-Light supercomputer. The solver of VTBE with the one-level restricted additive Schwarz preconditioner shows very good strong and weak scalabilities. For the solver of PPBE, a noticeable improvement in the computational efficiency and the weak scalability by the two-level preconditioner is observed, comparing to the one-level method.

To extend our code to the full dynamo problem, the implementations of the insulating boundary condition and the singularity in the inner core should be taken into consideration in the future. Possible solutions may include an integral boundary element approach (Iskakov et al., 2004) together with a parallel fast multipole method (Benson et al., 2014) for the issue of the insulating boundary condition and a logically rectangular grid suggested by (Calhoun et al., 2008)

for the inner core problem.

Acknowledgements

References

Aubert, J., 2019. Approaching Earths core conditions in high-resolution geo-dynamo simulations. Geophysical Journal International 219 (Supplement_1), S137–S151.

Aurnou, J. M., Calkins, M. A., Cheng, J. S., Julien, K., King, E. M., Nieves, D., Soderlund, K. M., Stellmach, S., 2015. Rotating convective turbulence in Earth and planetary cores. Physics of the Earth and Planetary Interiors 246, 52–71.

Balay, S., Brown, J., Buschelman, K., Eijkhout, V., Gropp, W. D., Kaushik, D., Knepley, M. G., McInnes, L. C., Smith, B. F., Zhang, H., 2013. PETSc Users Manual. Tech. Rep. ANL-95/11–Revision 3.4, Argonne National Laboratory.

Benson, A. R., Poulson, J., Tran, K., Engquist, B., Ying, L., 2014. A parallel directional fast multipole method. SIAM Journal on Scientific Computing 36 (4), C335–C352.

Cai, X.-C., Sarkis, M., 1999. A restricted additive Schwarz preconditioner for general sparse linear systems. SIAM Journal on Scientific Computing 21 (2), 792–797.

Calhoun, D. A., Helzel, C., LeVeque, R. J., 2008. Logically rectangular grids and finite volume methods for PDEs in circular and spherical domains. SIAM Review 50 (4), 723–752.

Chan, K. H., Li, L.-G., Liao, X.-H., 2006. Modelling the core convection using finite element and finite difference methods. Physics of the Earth and Planetary Interiors 157 (1), 124–138.

Chan, K. H., Zhang, K.-K., Li, L.-G., Liao, X.-H., 2007. A new generation of convection-driven spherical dynamos using EBE finite element method. Physics of the Earth and Planetary Interiors 163 (1), 251–265.

Chan, K. H., Zhang, K.-K., Zou, J., Schubert, G., 2001a. A non-linear, 3-D spherical α^2 dynamo using a finite element method. Physics of the Earth and Planetary Interiors 128 (1), 35–50.

Chan, K. H., Zhang, K.-K., Zou, J., Schubert, G., 2001b. A nonlinear vacillating dynamo induced by an electrically heterogeneous mantle. Geophysical Research Letters 28 (23), 4411–4414.

Chorin, A. J., 1968. Numerical solution of the Navier-Stokes equations. Mathematics of Computation 22, 745–762.

Christensen, U. R., 2018. Geodynamo models with a stable layer and heterogeneous heat flow at the top of the core. Geophysical Journal International 215 (2), 1338–1351.

Christensen, U. R., Aubert, J., Cardin, P., Dormy, E., Gibbons, S., Glatzmaier, G. A., Grote, E., Honkura, Y., Jones, C., Kono, M., Matsushima, M., Sakuraba, A., Takahashi, F., Tilgner, A., Wicht, J., Zhang, K.-K., 2001. A numerical dynamo benchmark. Physics of the Earth and Planetary Interiors 128 (1), 25–34.

Christensen, U. R., Wicht, J., 2007. Numerical dynamo simulations. In: Core Dynamics. Elsevier, pp. 245–282, edited by Olson, P. and Schbert, G.

Deguen, R., Lasbleis, M., 2020. Fluid dynamics of Earth's core: Geodynamo, inner core dynamics, core formation. In: Fluid Mechanics of Planets and Stars. Springer, pp. 129–212.

Demmel, J. W., 1997. Applied Numerical Linear Algebra. SIAM.

Dukowicz, J. K., Dvinsky, A. S., 1992. Approximate factorization as a high order splitting for the implicit incompressible flow equations. Journal of Computational Physics 102 (2), 336–347.

Fu, H.-H., Liao, J.-F., Yang, J.-Z., Wang, L.-N., Song, Z.-Y., Huang, X.-M., Yang, C., Xue, W., Liu, F.-F., Qiao, F.-L., Zhao, W., Yin, X.-Q., Hou, C.-F., Zhang, C.-L., Ge, W., Zhang, J., Wang, Y.-G., Zhou, C.-B., Yang, G.-W., 2016. The Sunway TaihuLight supercomputer: system and applications. Science China Information Sciences 59, 1–16.

Glatzmaier, G. A., 2002. Geodynamo simulations-how realistic are they? Annual Review of Earth and Planetary Sciences 30 (1), 237–257.

Glatzmaier, G. A., Roberts, P. H., 1995. A three-dimensional self-consistent computer simulation of a geomagnetic field reversal. Nature 377 (6546), 203–209.

Guermond, J. L., Minev, P., Shen, J., 2006. An overview of projection methods for incompressible flows. Computer Methods in Applied Mechanics and Engineering 195 (44), 6011–6045.

Harder, H., Hansen, U., 2005. A finite-volume solution method for thermal convection and dynamo problems in spherical shells. Geophysical Journal International 161 (2), 522–532.

Hejda, P., Reshetnyak, M., 2003. Control volume method for the dynamo problem in the sphere with the free rotating inner core. Studia Geophysica et Geodaetica 47 (1), 147–159.

Hejda, P., Reshetnyak, M., 2004. Control volume method for the thermal convection problem in a rotating spherical shell: test on the benchmark solution. Studia Geophysica et Geodaetica 48 (4), 741–746.

Iskakov, A. B., Descombes, S., Dormy, E., 2004. An integro-differential formulation for magnetic induction in bounded domains: boundary element–finite volume method. Journal of Computational Physics 197 (2), 540–554.

Jackson, A., Sheyko, A., Marti, P., Tilgner, A., Cébron, D., Vantieghem, S., Simitev, R., Busse, F., Zhan, X., Schubert, G., Takehiro, S., Sasaki, Y., Hayashi, Y.-Y., Ribeiro, A., Nore, C., Guermond, J.-L., 2014. A spherical shell numerical dynamo benchmark with pseudo-vacuum magnetic boundary conditions. Geophysical Journal International 196 (2), 712–723.

Jones, C. A., 2011. Planetary magnetic fields and fluid dynamos. Annual Review of Fluid Mechanics 43, 583–614.

Kageyama, A., Sato, T., 1995. Computer simulation of a magnetohydrodynamic dynamo. II. Physics of Plasmas 2 (5), 1421–1431.

Kageyama, A., Sato, T., 1997. Generation mechanism of a dipole field by a magnetohydrodynamic dynamo. Physical Review E 55 (4), 4617–4626.

Kageyama, A., Yoshida, M., 2005. Geodynamo and mantle convection simulations on the Earth Simulator using the Yin-Yang grid. In: Journal of Physics: Conference Series. Vol. 16. IOP Publishing, pp. 325–338.

Kuang, W.-J., Bloxham, J., 1997. An Earth-like numerical dynamo model. Nature 389 (6649), 371–374.

Mandel, J., 1994. Hybrid domain decomposition with unstructured subdomains. In: Domain Decomposition Methods in Science and Engineering: The Sixth International Conference on Domain Decomposition, Contemporary Mathematics. Vol. 157. American Mathematical Soc., pp. 103–112.

Matsui, H., Heien, E., Aubert, J., Aurnou, J. M., Avery, M., Brown, B., Buffett, B. A., Busse, F., Christensen, U. R., Davies, C. J., Featherstone, N., Gastine, T., Glatzmaier, G. A., Gubbins, D., Guermond, J.-L., Hayashi, Y.-Y., Hollerbach, R., Hwang, L. J., Jackson, A., Jones, C. A., Jiang, W.-Y., Kellogg, L. H., Kuang, W.-J., Landeau, M., Marti, P. H., Olson, P., Ribeiro, A., Sasaki, Y., Schaeffer, N., Simitev, R. D., Sheyko, A., Silva, L., Stanley, S., Takahashi, F., Takehiro, S., Wicht, J., Willis, A. P., 2016. Performance benchmarks for a next generation numerical dynamo model. Geochemistry, Geophysics, Geosystems 17 (5), 1586–1607.

Matsui, H., Okuda, H., 2002. Thermal convection analysis in a rotating shell by a parallel finite-element method–development of a thermal-hydraulic subsystem of GeoFEM. Concurrency and Computation: Practice and Experience 14 (6–7), 465–481.

Matsui, H., Okuda, H., 2004a. Development of a simulation code for MHD dynamo processes using the GeoFEM platform. International Journal of Computational Fluid Dynamics 18 (4), 323–332.

Matsui, H., Okuda, H., 2004b. MHD dynamo simulation using the GeoFEM platform: comparison with a spectral method. Pure and Applied Geophysics 161 (11–12), 2199–2212.

Matsui, H., Okuda, H., 2005. MHD dynamo simulation using the GeoFEM platform–verification by the dynamo benchmark test. International Journal of Computational Fluid Dynamics 19 (1), 15–22.

Moffatt, K., Dormy, E., 2019. Self-Exciting Fluid Dynamos. Vol. 59. Cambridge University Press.

Petitdemange, L., 2018. Systematic parameter study of dynamo bifurcations in geodynamo simulations. Physics of the Earth and Planetary Interiors 277, 113–132.

Roberts, P. H., King, E. M., 2013. On the genesis of the Earth's magnetism. Reports on Progress in Physics 76 (9), 096801.

Ronchi, C., Iacono, R., Paolucci, P. S., 1996. The cubed sphere: a new method for the solution of partial differential equations in spherical geometry. Journal of Computational Physics 124 (1), 93–114.

Saad, Y., 2003. Iterative Methods for Sparse Linear Systems, 2nd Edition. SIAM.

Sadourny, R., 1972. Conservative finite-difference approximations of the primitive equations on quasi-uniform spherical grids. Monthly Weather Review 100 (2), 136–144.

Sheyko, A., 2014. Numerical investigations of rotating MHD in a spherical shell. Ph.D. thesis, ETH Zürich.

Sheyko, A., Finlay, C. C., Jackson, A., 2016. Magnetic reversals from planetary dynamo waves. Nature 539 (7630), 551–554.

TOP500, 2020. Top 500 supercomputer sites. `http://www.top500.org`.

Toselli, A., Widlund, O. B., 2005. Domain Decomposition Methods – Algorithms and Theory. Springer.

Tóth, G., 2000. The $\nabla \cdot \mathbf{B} = 0$ constraint in shock-capturing magnetohydrodynamics codes. Journal of Computational Physics 161 (2), 605–652.

Vantieghem, S., Sheyko, A., Jackson, A., 2016. Applications of a finite-volume algorithm for incompressible MHD problems. Geophysical Journal International 204 (2), 1376–1395.

Wicht, J., Stellmach, S., Harder, H., 2009. Numerical models of the geodynamo: From fundamental Cartesian models to 3D simulations of field reversals. In: Geomagnetic Field Variations. Springer, pp. 107–158.

Wicht, J., Tilgner, A., 2010. Theory and modeling of planetary dynamos. Space Science Reviews 152 (1–4), 501–542.

Yang, C., Cai, X.-C., 2011. Parallel multilevel methods for implicit solution of shallow water equations with nonsmooth topography on the cubed-sphere. Journal of Computational Physics 230 (7), 2523–2539.

Yin, L., Yang, C., Ma, S.-Z., Huang, J.-Z., Cai, Y., 2017. Parallel numerical simulation of the thermal convection in the Earth's outer core on the cubed-sphere. Geophysical Journal International 209 (3), 1934–1954.

Yin, L., Yang, C., Ma, S.-Z., Zhang, K.-K., 2019. Parallel and fully implicit simulations of the thermal convection in the Earth's outer core. Computers & Fluids 193, 104278.

Zhang, K., Schubert, G., 2000. Magnetohydrodynamics in rapidly rotating spherical systems. Annual Review of Fluid Mechanics 32 (1), 409–443.